A&A 456, 409–420 (2006)
DOI: 10.1051/0004-6361:20053384

Astronomy & Astrophysics

VIMOS-IFU survey of $z \sim 0.2$ massive galaxy clusters

I. Observations of the strong lensing cluster Abell 2667⋆

G. Covone[1], J.-P. Kneib[1,2], G. Soucail[3], J. Richard[3,2], E. Jullo[1], and H. Ebeling[4]

[1] OAMP, Laboratoire d'Astrophysique de Marseille, UMR 6110, traverse du Siphon, 13012 Marseille, France
e-mail: giovanne.covone@na.astro.it
[2] Caltech-Astronomy, MC105-24, Pasadena, CA 91125, USA
[3] Observatoire Midi-Pyrénées, CNRS-UMR 5572, 14 avenue E. Belin, 31400 Toulouse, France
[4] Institute for Astronomy, University of Hawaii, 2680 Woodlawn Dr, Honolulu, HI 96822, USA

Received 9 May 2005 / Accepted 21 December 2005

ABSTRACT

We present extensive multi-color imaging and low-resolution VIMOS integral field unit (IFU) spectroscopic observations of the X-ray luminous cluster Abell 2667 ($z = 0.233$). An extremely bright giant gravitational arc ($z = 1.0334 \pm 0.0003$) is easily identified as part of a triple image system, and other fainter multiple images are also revealed by the *Hubble Space Telescope* Wide Field Planetary Camera-2 images. The VIMOS-IFU observations cover a field of view of $54'' \times 54''$ and enable us to determine the redshift of all galaxies down to $V_{606} = 22.5$. Furthermore, redshifts could be identified for some sources down to $V_{606} = 23.2$. In particular we identify 21 members in the cluster core, from which we derive a velocity dispersion of $\sigma = 960^{+190}_{-120}$ km s^{-1}, corresponding to a total mass of $7.1 \pm 1.8 \times 10^{13}\, h_{70}^{-1}\, M_\odot$ within a $110\, h_{70}^{-1}$ kpc (30 arcsec) radius. Using the multiple images constraints and priors on the mass distribution of cluster galaxy halos we construct a detailed lensing-mass model leading to a total mass of $2.9 \pm 0.1 \times 10^{13}\, h_{70}^{-1}\, M_\odot$ within the Einstein radius (16 arcsec). The lensing mass and dynamical mass are in good agreement, although the dynamical one is much less accurate. Within a $110\, h_{70}^{-1}$ kpc radius, we find a rest-frame K-band M/L ratio of $61 \pm 5\, h_{70}\, M_\odot/L_\odot$. Comparing these measurements with published X-ray analysis is, however, less conclusive. Although the X-ray temperature matches the dynamical and lensing estimates, the published NFW mass model derived from the X-ray measurement with its low concentration of $c \sim 3$ cannot account for the large Einstein radius observed in this cluster. A higher concentration of ∼6 would, however, match the strong lensing measurements. These results very likely reflect the complex structure of the cluster mass distribution, underlying the importance of panchromatic studies from small to large scale in order to better understand cluster physics.

Key words. gravitational lensing – galaxies: clusters: general – galaxies: clusters: individual: Abell 2667

1. Introduction

Massive galaxy clusters offer an important laboratory for investigating the evolution and formation of the galaxies and the large scale structure of the Universe (see, e.g., the historical review of the study of galaxy clusters along the last two centuries in Biviano 2000) and act as natural telescopes by magnifying the distant galaxy population. Indeed, the most massive clusters are dense enough to have a central-surface mass density that is larger than the critical density for strong lensing. This means that multiple images of background sources can be observed, and in some rare cases when the source position is close to the caustics, highly magnified multiple images can be observed as giant luminous arcs. It is precisely by observing these rare events that cluster lensing was discovered (Lynds & Petrosian 1986; Soucail et al. 1987, 1988).

Hence, the discovery of a giant luminous arc in a galaxy cluster is direct evidence of a very dense core, and it also corresponds to a rare opportunity for studying the physical properties of intrinsically faint sources in the high-z Universe in greater details, since the magnification factor is generally higher than 10 (e.g. Ellis et al. 2001; Kneib et al. 2004a,b; Egami et al. 2005).

On the other hand, the accurate estimates of cluster mass distribution obtained by using strong and weak lensing can be compared to numerical predictions of the cold dark matter scenarios (e.g. Kneib et al. 2003; Sand et al. 2004; Broadhurst et al. 2005). In some cases where multiple images with spectroscopic redshift have been identified in a set of well-modeled clusters, it is possible to put significant constraints on the cosmological parameters (Soucail et al. 2004).

Wide-field integral-field spectroscopy (IFS) is a novel observing technique with straightforward and important applications in the observations of galaxy clusters. Indeed, IFS provides a tool for efficiently obtaining complete spectroscopic information in a contiguous sky area without the multiplexing difficulties of multi-object spectroscopy, and, mostly important, without the need of a priori selecting the targets to be observed. For instance, this technique can probe rich clusters at $z \sim 1$ in the early stages of their formation to obtain a complete (spatially and in magnitude) survey of the galaxy population in the inner and denser regions.

An important application to massive clusters at intermediate redshift is the survey of the critical lines in the cluster cores to identify gravitationally lensed objects. We have

⋆ Based on observations made with ESO telescopes at the Paranal Observatories (programs ID 71.A-3010 and 71.A-0428) and on observations made with the NASA/ESA Hubble Space Telescope, obtained from the data archive at the Space Telescope Institute. STScI is operated by the association of Universities for Research in Astronomy, Inc. under the NASA contract NAS 5-26555.

thus started an IFS survey of the critical lines in a sample of eight massive galaxy clusters using the VIsible Multi-Object Spectrograph (VIMOS, Le Fèvre et al. 2003) Integral Field Unit (IFU), mounted on VLT Melipal, both in low and high spectral resolution ($R \sim 200$ and 2500, respectively). The cluster sample was selected among X-ray bright, lensing clusters at redshift $z \simeq 0.2$, for which *Hubble Space Telescope* (*HST*) high-resolution imaging and *Chandra/XMM-Newton* X-ray observations are already available.

The main scientific goals of this project are (i) to search for and physically characterize low-mass, highly magnified star-forming galaxies (see, e.g., Campusano et al. 2001), (ii) to use strong lensing clusters to constrain the cosmological parameters, as explained by Golse et al. (2002), and to study the evolution of the early-type galaxy population in the rich cluster cores (Covone et al. 2006a).

In this paper, we present the first results from this IFS survey: new VIMOS-IFU observations and a multi-wavelength imaging analysis of Abell 2667 ($\alpha_{J2000} = 23^{\rm h}51^{\rm m}39.4^{\rm s}$, $\delta_{J2000} = -26^{\rm o}05'02''.8$), a remarkable cluster from the selected sample. In this work we focus on the mass model of this cluster using both strong gravitational lensing and a dynamical analysis of the cluster core. In a forthcoming paper we will present a detailed multi-wavelength analysis of the giant gravitational arc and the other lensed high-z galaxies.

Abell 2667 is a distance class-6, richness class-3 cluster in the Abell catalog (Abell 1958), with the cD galaxy located at redshift $z = 0.233$. Although expected to be an X-ray bright source and to be detected in the *ROSAT* All-Sky Survey, Abell 2667 is not listed in the X-ray flux limited XBACs sample of Ebeling et al. (1996). The reason for this omission is an unusually large offset of the X-ray position from the optical cluster centroid listed in the Abell catalog. Abell 1967 was then serendipitously detected during *ROSAT* PSPC observations of the nova-like star V★ VZ Scl in December 1992, when the X-ray centroid of the cluster was found to be more than 5′ off the nominal Abell position. It is this X-ray observation of Abell 2667 that has motivated observers to include this object in their optical/X-ray follow-up observations. In particular, a giant luminous arc was easily identified in the cluster core (Rizza et al. 1998; Ebeling et al., in preparation). Remarkably, this arc is so bright that it is detected on DSS2 images, although not recognized as an arc. Using the LRIS spectrograph on the Keck-2 10-m telescope in August 1997 and October 1998, Ebeling et al. (in preparation) obtained long-slit spectra of both knots in the giant arc, as well as of the third image. These observations identified the triple arc as a galaxy at a redshift of $z = 1.034 \pm 0.005$ based on a strong [OII] emission line. More recently, a new Keck long-slit optical spectrum of this arc was obtained by Sand et al. (2005), with the same redshift identification.

Abell 2667 is among the most luminous galaxy clusters known in the X-ray sky. The *ROSAT* HRI observations give an X-ray luminosity[1] (in the 0.1−2.4 keV band) of $14.90 \pm 0.56 \times 10^{44}\, h_{70}^{-2}$ erg s^{-1} and show a regular X-ray morphology suggestive of a relaxed dynamical state (Allen et al. 2003). Using the same data, Rizza et al. (1998) estimated a cooling flow time $t_{\rm cool} = 1.8 \times 10^9$ yrs (much smaller than the age of the Universe at the cluster redshift), and detected the presence of a substructure in the intra-cluster medium, as proved by the shift of 6.0 ± 2.0 arcsec in the X-ray surface brightness centroid position between the regions in and outside a radius of 150 kpc.

The brightest cluster galaxy is also a powerful radio source with radio flux density $S = 20.1$ mJy at 1.4 Ghz, as measured in the NRAO VLA sky survey (Condon et al. 1998). This galaxy was also included in the sample of radio-emitting X-ray sources observed by Caccianiga et al. (2000). They found strong optical nebular emission lines and classified this source as a narrow emission-line AGN; i.e., all the observed emission lines have *FWHM* lower than 1000 km s^{-1} in the source rest frame. More recently, Allen et al. (2003) used *Chandra* data to estimate the mass of this cluster: by fitting a Navarro-Frenk-White (1996, NFW) model, they found $M_{200} = 13.6^{+10.6}_{-4.6}\, 10^{14}\, h_{70}^{-1}\, M_\odot$, within a virial radius of r_{200} and with a concentration $c = 3.0 \pm 0.8$. Fukazawa et al. (2004) have measured an X-ray temperature of 6.15 ± 0.61 keV (excluding the central, cool region), based on *ASCA* observations. Using archive *ROSAT* and *ASCA*, Ota & Mitsuda (2004) obtained a new measurement of the X-ray temperature found to be $5.95^{+0.42}_{-0.23}$ keV.

The outline of the paper is the following. We present the IFU observations in Sect. 2, along with the other supporting imaging observations. The IFU data reduction and analysis are presented in Sect. 3. Section 4 presents the catalog and the spectroscopic information derived from the IFU data, and Sect. 5 treats the lensing and dynamical mass models and compares them with recent mass estimates based on X-ray observations. Finally, the main results are summarized in Sect. 6. In the following, magnitudes are given in the AB system.

2. Observations

2.1. Imaging data

Abell 1967 was observed on October 10−11, 2001 with the *HST* using the WFPC2 in the *F450W* (5×2400 s), *F606W* (4×1000 s), and *F814W* (4 × 1000 s) filters (PI: Allen, proposal ID: 8882). Images were retrieved from the ST-ECF archive and reduced using the IRAF `drizzle` package (Fruchter & Hook 2002). The final spatial resolution of the images is 0.″05 per pixel. Figure 1 shows a color image of the cluster core made of the 3 *HST* images: the giant luminous arc is very prominent, and other new candidate multiple images systems (see discussion in Sect. 5) are indicated. The 5σ limit detection for point sources on the final images is 24.76, 25.44, and 24.61 in the filters *F450W*, *F606W*, and *F814W*, respectively.

On 30 May and 1st June 2003, near-infrared J and H-band observations with ISAAC were obtained with the *Very Large Telescope* (*VLT*) (as part of program ID: 71.A-0428, PI: Kneib) under photometric sky conditions. The total exposure time for the J-band and H-band ISAAC data are 7932 s ($34.8 \times 4 \times 57$ s) and 6529 s ($11.4 \times 10 \times 57$ s), respectively. The data were reduced using standard IRAF scripts, and the final PSF is 0.″51 and 0.″58 in the J-band and in the H-band, respectively (pixel scale is 0.″148 per pixel). The measured 5σ detection limit for point sources are 25.6 and 24.7 in J and H, respectively.

2.2. VIMOS-IFU 3D spectroscopy

The integral field spectrograph is one of the three operational modes available on VIMOS (Le Fèvre et al. 2003). The IFU consists of 4 quadrants of 1600 fibers each, feeding four different 2k × 4k CDDs. Each quadrant is made by four sets (pseudo-slits) of 400 fibers. To date, the VIMOS-IFU is the integral field spectrograph with the largest field of view (f.o.v.), among

[1] Throughout this paper we assume a cosmological model with $\Omega_{\rm m} = 0.3$, $\Omega_\Lambda = 0.7$, and $H_0 = 70\, h_{70}$ km s^{-1} Mpc^{-1}. At $z = 0.233$ the angular scale is thus 3.722 kpc arcsec^{-1}.

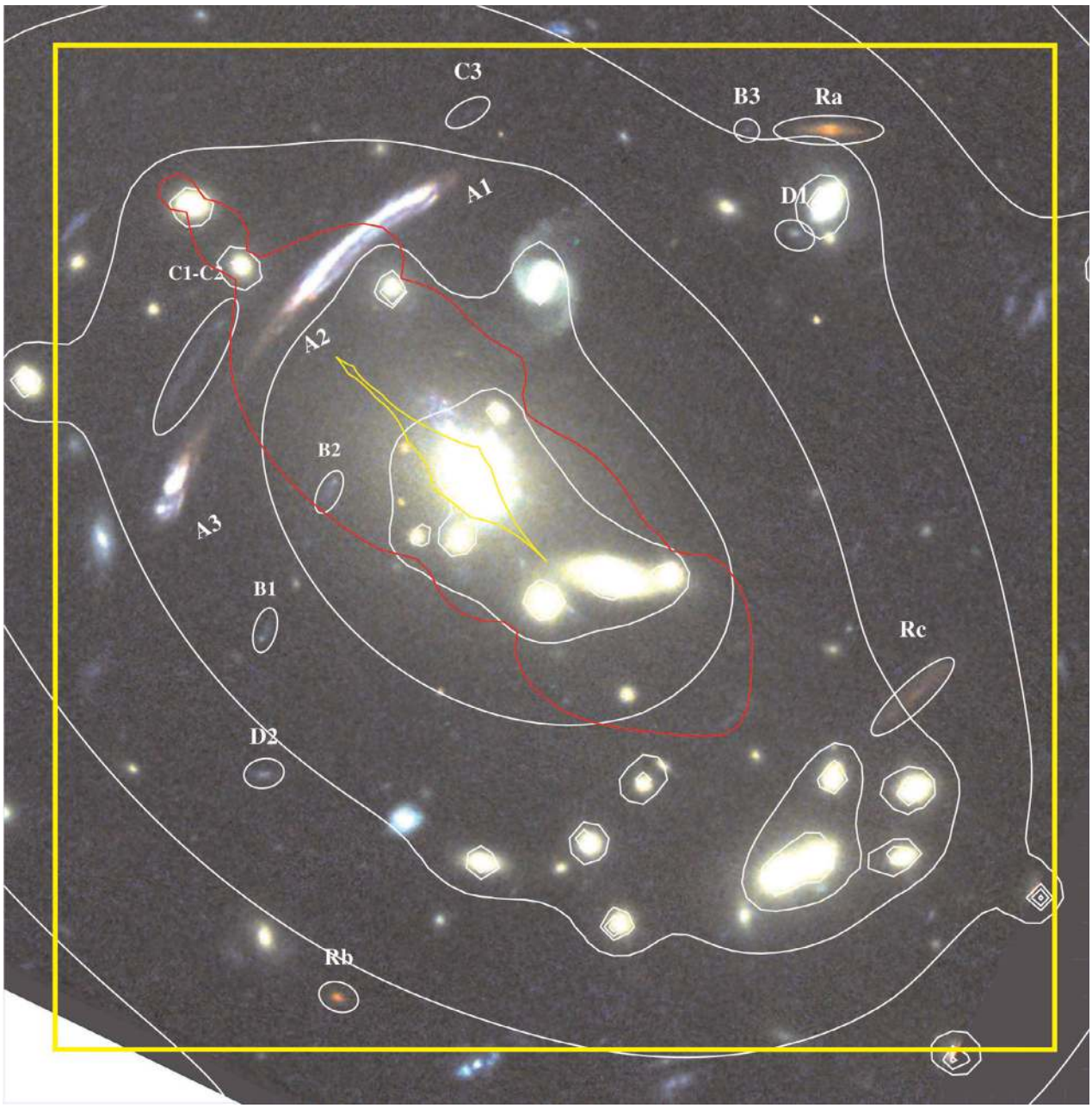

Fig. 1. Color image of the Abell 2667 cluster core imaged with *HST* in the *F450W*, *F606W*, and *F814W* filters. The thin yellow square represents the position of the IFU field-of-view. Note the strongly magnified gravitational arc and the extended blue region just NE of the central galaxy. The white lines correspond to iso-mass contours from the lens model; the red line is the critical line at the redshift of the giant arc. High-z objects discussed in the text are also marked. North is at the top, East to the left. The field of view is centered on α_{J2000} = 23:51:39.4, δ_{J2000} = −26:05:03. At a redshift of $z = 0.233$, the angular scale is 3.722 kpc/arcsec.

those available on 8/10-m class telescopes. The f.o.v. covers (in the lower spatial resolution mode) a contiguous sky region of $54'' \times 54''$, with 6400 fibers of $0.''66$ diameter. The dead space between adjacent fibers is less than 10% of the fiber dimension.

The galaxy cluster Abell 2667 was observed in service mode on the nights 29 and 30 June 2003 (as part of program ID: 71.A-3010, PI: Soucail). Both nights were photometric, with the DIMM seeing varying between $0.''6$ and $0.''8$ during the observations of the cluster, performed at an airmass always lower than 1.28. We used the spatial low-resolution mode (fibers with diameter $0.''66$) and the low-resolution blue grism (LR-B) in combination with an order-sorting filter, which covers the wavelength range from 3500 Å to 7000 with spectral resolution $R \sim 250$ and dispersion of 5.355 Å/pixel. However, because of the spectra overlapping between contiguous pseudo-slits on the CCD, the first and last ≃50 pixels on the raw spectra from most of the pseudo-slits are not usable. This reduces the useful spectral range approximatively from 3900 to 6800 Å.

The overall exposure time was 10.8 ks (4×2700 s, two exposures were obtained each night). A small offset of about 2 arcsec among consecutive exposures has been applied, in order to compensate the non uniform efficiency of the fibers and the presence of a small set of low-quality fibers.

Calibration frames were obtained soon after each one of the 4 exposures, and a spectrophotometric standard star was observed each night. The final area is $54.''8 \times 55.''4$, corresponding

to a region of about 200×200 kpc^2, centered 5″ SW from the brightest cluster galaxy.

3. Reduction of the VIMOS-IFU data

The whole reduction process of the VIMOS-IFU data was completed using the VIMOS Interactive Pipeline Graphical Interface (VIPGI, Scodeggio et al. 2005), a tool dedicated to handling and reducing VIMOS data[2]. A description of the data reduction methods and data quality assesment can be found in Zanichelli et al. (2005). Every reduction step before the final combination of the dithered exposures in a single data cube is performed on a single-quadrant basis. The main steps are the followings: check and adjust the so-called *first guesses* of the instrumental model (see below), create of the spectra extraction tables at each pointing, preprocess CCD, perform wavelength calibration, remove cosmic ray hits, determination of fiber efficiency, subtracte the sky background and perform flux calibration.

The VIMOS-IFU data reduction requires a highly accurate description of the optical and spectral distortions of the instrument, especially for the spectra location and the wavelength. These distortions are modeled using third-order polynomials, whose coefficients (as periodically determined by the staff at the telescope) are stored in the raw FITS file headers. However, since these distortions may change in time (because of, e.g., the different orientation of the instrument during observation or the instrument aging), such a predefined model can only be used as a first guess when calibrating the scientific frames. Moreover, we experienced that most of the time these first guesses are not close enough to the actual instrument distortions to be safely used, mainly because of the large flexure of the instrument between the time of their definition and the time of observation (see, e.g., D'Odorico et al. 2003). These differences can add up to a few pixels (see, e.g., D'Odorico et al. 2003), and are larger for observations at the meridian and close to the zenith, as in the present case. Therefore, the original first guesses for the spectra location and the inverse dispersion law need to be checked and corrected for any given pointing by using the calibration frames as close in time as possible to the scientific exposures and taken at the same rotator's absolute position. For this purpose, we used a specific, graphically guided tool provided in VIPGI to interactively correct the polynomial coefficients describing the optical and wavelength distortions (Scodeggio et al. 2005), independently for each calibration set associated to the scientific exposures. These corrected values are then used in the following location of spectra traces and wavelength calibration.

Having adjusted the first guesses for the optical distortions, it is then possible to trace the spectra of the 4 detectors. Location of the spectra traces is a very critical step, since spectra are highly packed on the CCDs: distances between spectra from contiguous fibers are 5 pixels, each fiber having a *FWHM* of ≃3.2 pixels. Therefore, even small errors (∼1 pixel) in tracing the exact position of the spectra can result in a degraded quality for the final result. Because of their high S/N, we have used flat field lamps taken immediately after each scientific exposure to trace the spectra. In this step an extraction table is created, which is then used to trace spectra of the scientific exposures. The accuracy of the extraction tables was visually checked on the raw scientific frame themselves by verifying that the fibers with highest signal are indeed traced correctly.

[2] VIPGI has been developed within the VIRMOS Consortium. See the VIPGI web site for more information: `http://cosmos.mi.iasf.cnr.it/marcos/vipgi/vipgi.html`

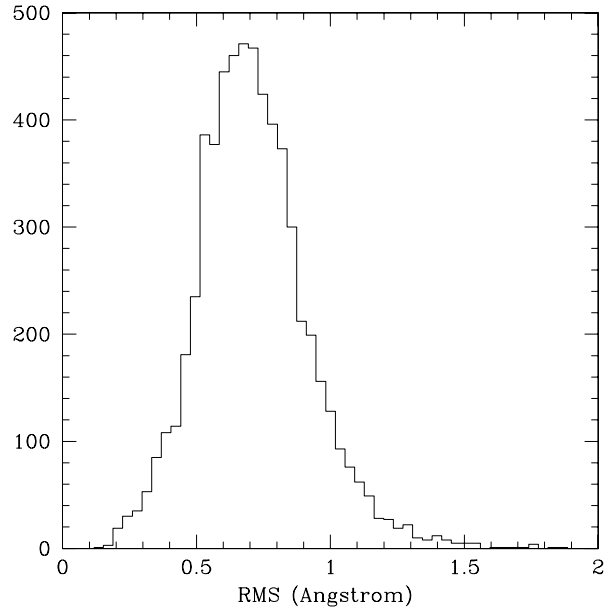

Fig. 2. Distribution of the rms residuals in the wavelength calibration for all the useful fibers in the first pointing. The median value is 0.716 Å, i.e. 0.15 pixel. 95% of the fiber has rms lower than 1.0 Å.

Because of the high density of the spectra on the VIMOS detectors, there is a non negligible amount of crosstalk, i.e., flux contamination among nearby fibers. However, we made no attempt to correct for this effect: correcting for the cross-talk would indeed need very good modeling of the fiber profile in the cross-dispersion direction. Zanichelli et al. (2005) show that the average contamination on each neighboring fiber is ∼5%, i.e. smaller or the same order of magnitude as the error introduced by fitting the fiber profile, since the quality of crosstalk correction decreases rapidly as soon as the error on the width measurements is on the order of ≃0.2 pixels.

The inverse dispersion law is calculated starting from the adjusted first guesses and a fit by a third-order polynomial function. All the inverse dispersion solutions were visually checked by comparing the predicted positions of arc lamp lines (Neon and Helium lamps) with their effective positions on raw frames. To demonstrate the accuracy of the wavelength calibration, the distribution of the rms residuals in the wavelength calibration for the 6400 fibers in a single pointing is plotted in Fig. 2, and the median value is 0.716 Å, i.e. about 0.15 pixels, with negligible differences among the four quadrants.

The scientific exposures were overscan-trimmed and bias-subtracted, and cosmic ray hits were cleaned. The cleaning algorithm (described in Zanichelli et al. 2005) was based on a sigma-clipping method and dependes on the fact that along the dispersion direction spectra with strong emission lines also show a smooth behavior, while comics rays show very strong gradients. This method is very efficient in removing hits spanning only a few pixels (∼99%), and has lower efficiency (∼90%) only in the case of more extended ones. A further cleaning has therefore been applied in the final combination of the dithered exposures.

Finally, the wavelength calibration was applied and the 1D-spectra extracted. Extraction of the spectra was based on the Horne's (1986) recipe. At this stage sky lines were used to check and refine the wavelength calibration, in order to compensate for the effects of possible further differential flexure between the lamp and scientific exposures.

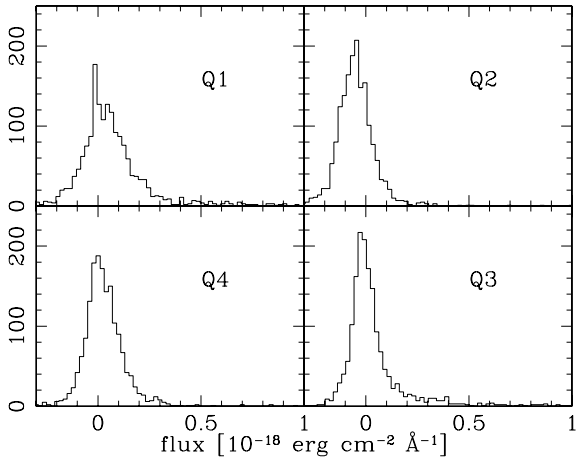

Fig. 3. Distribution of the average fiber flux values between 4000 and 6200 Å in the four quadrants of the fully reduced data-cube, showing the uniformity of the background in the different quadrants. In all quadrants, distributions are centered around zero, with standard deviation $0.7-1.1 \times 10^{18}$ erg cm^{-2} Å^{-1} s^{-1}.

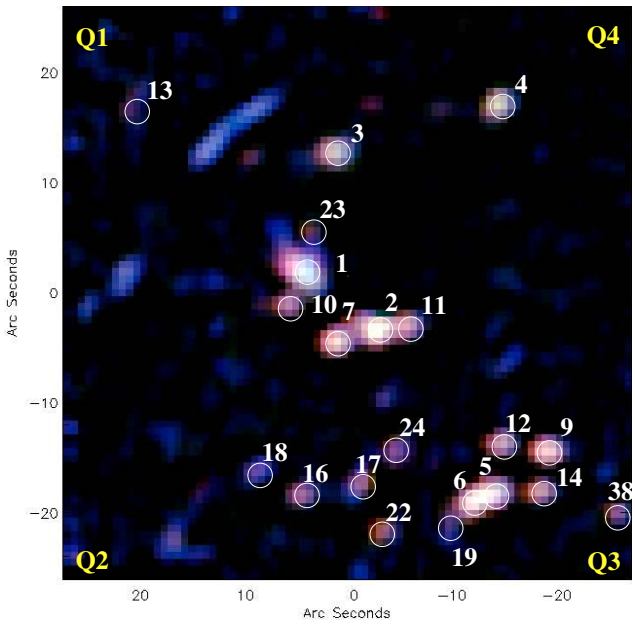

Fig. 4. VIMOS-IFU bi-dimensional color image of the central region of the cluster Abell 2667. The blue, green, and red color channels were built by averaging the flux in the spectral ranges: 4500–4700 Å, 4900–5400 Å, and 5700–6200 Å, respectively. The orientation is the same as in Fig. 1. The blue region just NE of the cD galaxy corresponds to an extended emission-line region at the same redshift as the cD. The 21 galaxies with secure redshift measurement (excluding the lensed sources A and Ra) are identified in the plot.

Then, the correction of the fiber-to-fiber relative transmission (analogous to the flat-fielding in the imaging case) is done by measuring the flux in each 1D spectrum contained in a user-specified strong sky line, either the 5577 Å or the 5892 Å lines. We calculated the relative transmission of each fiber independently in 16 different exposures, with the given grism performed in the present observing run and used its median value.

Since VIMOS-IFU does not have a dedicated set of fibers for determining the sky background level, sky subtraction was performed in a statistical way: in each module, fibers are grouped in three sets according to their shape (as characterized by the *FWHM* and skewness of the fiber output on the CCD), and the sky level is obtained by their mode (Scodeggio et al. 2005). This approach gives robust results when applied to a field in which most of the fibers only have a sky signal, as in the present case.

Flux calibration is done separately for each quadrant of single exposures, using the observations of a standard star. A sequence of observations with the star centered on each quadrant, respectively, is taken each night. From comparing the flux-calibrated spectra with the B_{450} and V_{606} magnitudes, we estimated the accuracy of the spectrophotometric calibration to be ∼20%.

Finally, the four fully reduced exposures were combined together by using shifts of an integer number of fibers. The final data cube was corrected for the effect due to the differential atmospheric refraction using the formula from Filippenko (1982) and converted to the Euro3D FITS data format (Kissler-Patig et al. 2004).

The final data cube is made of 6806 spatial elements, each one representing a spectrum going from ≃3900 to 6800 Å; it covers a sky area of 0.83 arcmin^2, centered 5″ arcsec South-West of the brightest cluster galaxy. The median spectral resolution is ≃18 Å, as estimated from Gaussian fits to sky lines in the final data-cube. The 3D-cube was explored and analyzed by using the visualization tool E3D (Sánchez 2004) and specific IDL programs written by the authors. In Fig. 3 we plot the average flux distribution of all the 6806 spatial elements of the final data-cube. The four IFU quadrant show good uniformity in terms of sky background level and noise, and the flux distribution is described very well by a Gaussian peaked around zero, with a small tail representing the fibers located on detected objects. The overall sky background subtraction is relatively accurate, as the background level in the final data-cube is around zero in the blank sky regions at all wavelengths. However, the root-mean-square fluctuations of the background are a strong function of the sky position and the wavelength, as further discussed in Sect. A. Finally, a major limitation above ∼6200 Å is given by the zero order contaminations, whose position changes from one pseudo-slit to the other and from quadrant to quadrant.

A bi-dimensional color projection of the data-cube is shown in Fig. 4. In this image, the blue, green, and red color channels were built by averaging the flux in the following spectral ranges: 4500–4700 Å (therefore including the [OII] emission line at the cluster redshift), 4900–5400 Å (which covers the 4000 Å break at the cluster redshift), and 5700–6200 Å. The giant arc, which is characterized by a strong continuum emission, is remarkable at all wavelengths, and also the blue-emitting region around the central galaxy and the brightest cluster galaxies are easily recognized.

4. The catalog

The photometric catalog of objects within the VIMOS-IFU f.o.v. was built using SExtractor (Bertin & Arnouts 1996) on the χ^2-image obtained by combining the *HST F450W*- and *F606W*-band images (which overlap the spectral range of the VIMOS-IFU data). We used the Skycat GAIA tool to find the astrometric solution for the IFU data-cube in order to identify the fibers covering the detected objects. For each object, a 1D spectrum is obtained by summing the signal on all the associated fibers. We also searched the VIMOS-IFU data-cube directly for objects using a tool prepared by the authors (Covone et al., in preparation). One bright object (ID = 38) was detected in the IFU data-cube and has no *HST* counterpart since this falls

Table 1. Spectrophotometric catalog of the galaxies within the VIMOS-IFU f.o.v. Columns 4 and 7 list the total magnitudes B_{450} and J (AB system), while colors are measured on 2″ apertures. Flag represents quality of the redshift measurements (see text). In the last column, we specify the type of spectral features identified in the spectra.

ID	α(J2000)	δ(J2000)	B_{450}	$B-V$	$B-I$	J	$J-H$	z	Flag	Lines
1	23:51:39.4	–26:05:03.3	19.12	1.03	1.90	16.58	0.25	0.2345	4	abs, em
2	23:51:38.8	–26:05:08.8	20.34	1.56	2.33	17.32	0.21	0.2465	4	abs
3	23:51:39.1	–26:04:52.8	20.64	1.14	1.66	18.49	0.13	0.2233	4	abs
4	23:51:38.0	–26:04:48.2	20.90	1.24	1.89	18.43	0.14	0.1570	4	abs
5	23:51:38.0	–26:05:24.0	20.90	1.53	2.27	17.94	0.19	0.2346	4	abs
6	23:51:38.2	–26:05:24.8	20.93	1.47	2.20	18.00	0.19	0.2316	4	abs
7	23:51:39.1	–26:05:10.2	20.97	1.60	2.39	17.85	0.23	0.2316	4	abs
8	23:51:39.7	–26:04:53.2	21.06	1.31	1.97	18.73	0.10	0.2205	1	abs
9	23:51:37.6	–26:05:20.0	21.53	1.54	2.32	18.45	0.21	0.2338	4	abs
10	23:51:39.5	–26:05:06.8	21.73	1.47	2.21	18.79	0.20	0.2353	4	abs
11	23:51:38.6	–26:05:08.6	21.82	1.55	2.29	18.87	0.20	0.2309	4	abs
12	23:51:38.0	–26:05:19.4	21.86	1.56	2.31	18.73	0.21	0.2311	4	abs
13	23:51:40.6	–26:04:48.8	21.89	1.46	2.23	19.00	0.20	0.2333	2	abs
14	23:51:37.7	–26:05:23.8	21.94	1.51	2.27	18.94	0.19	0.2325	4	abs
15	23:51:40.3	–26:04:52.1	21.98	1.39	2.10	19.20	0.13	–	–	
16	23:51:39.4	–26:05:24.4	22.16	1.40	2.12	19.39	0.17	0.2447	2	abs
17	23:51:38.9	–26:05:23.3	22.22	1.43	2.12	19.44	0.15	0.2308	4	abs
18	23:51:39.7	–26:05:22.1	22.29	0.82	1.18	20.78	0.04	0.3980	3	em
19	23:51:38.3	–26:05:27.0	22.38	1.31	1.95	19.70	0.17	0.2290	2	abs
20	23:51:39.6	–26:05:06.7	22.48	1.48	2.20	19.64	0.20	0.2404	1	abs
21	23:51:40.9	–26:05:07.1	22.55	0.86	1.29	21.11	0.06	0.2140	1	abs, em
22	23:51:38.8	–26:05:27.6	22.60	1.60	2.37	19.47	0.22	0.2352	4	abs
23	23:51:39.3	–26:04:59.9	22.66	1.43	2.18	19.82	0.20	0.2360	3	abs, em
24	23:51:38.7	–26:05:20.0	22.94	1.50	2.23	19.98	0.18	0.2351	4	abs
25	23:51:40.2	–26:05:28.6	23.04	1.32	2.02	20.54	0.14	0.2255	1	abs
26	23:51:38.0	–26:04:50.1	23.40	1.10	1.73	21.04	0.14	–	–	–
27	23:51:37.1	–26:04:53.9	23.53	0.30	0.80	21.84	0.17	–	–	–
28	23:51:38.4	–26:04:48.6	23.58	1.19	1.88	21.27	0.07	0.2440	1	abs
29	23:51:39.1	–26:04:39.0	23.59	0.25	0.58	22.12	0.14	–	–	–
30	23:51:38.8	–26:05:15.1	23.77	1.51	2.19	20.96	0.12	0.2336	1	abs
31	23:51:39.3	–26:05:35.2	23.87	0.19	0.16	22.90	–0.23	–	–	–
32	23:51:41.0	–26:04:50.0	23.89	0.23	0.48	22.66	–0.44	–	–	–
33	23:51:39.7	–26:05:01.9	23.91	1.39	2.58	20.41	0.05	0.2380	1	abs
34	23:51:38.0	–26:04:54.6	24.28	0.69	0.99	23.58	–0.02	–	1	–
35	23:51:39.0	–26:05:24.6	24.51	1.42	2.19	21.46	0.10	0.2270	1	abs
36	23:51:37.3	–26:04:53.7	24.56	0.15	0.40	23.68	–0.33	–	–	–
37	23:51:40.8	–26:05:19.5	24.81	1.10	1.58	23.22	–0.09	–	–	–
38	23:51:37.1	–26:05:25.3	–	–	–	19.81	0.20	0.2301	3	abs

outside of the WFPC2 f.o.v. Finally, 39 objects were detected in the VIMOS-IFU data cube, an object being considered as detected if we could find at least a featureless continuum at the position of the *HST* object.

The redshifts were measured using a cross-correlation technique by means of the IRAF task `xcsao` (Kurtz et al. 1992), and visually checked by at least two of us. The median error on individual measurements is ∼0.0003, as estimated by using this software. The instrumental uncertainty is about ∼100 km s^{-1} in the rest frame. We assigned a confidence flag from 1 to 4, following Le Fèvre et al. (1995): flag 1 corresponds to a subjective probability of 50% that the line identification is correct, flag 2 to a probability of 75% (with more than one spectral feature identified), flag 3 to a probability higher than 95%, and flag 4 to an unquestionable identification.

We obtained redshift measurements for 34 objects, including 25 secure ones (i.e., confidence flag higher than 1). The faintest object for which we could measure the redshift has magnitude $B_{450} = 24.58$ (in a 2″ aperture). The final galaxy catalog is shown in Table 1, while information on the gravitationally lensed sources is given in Table 2. Table 1 contains photometric and spectroscopic information for the objects with a redshift measurement and photometric information for the remaining objects that are brighter than $B_{450} = 24.8$.

The overall efficiency of the redshift survey within the central region of A2667 is plotted in Fig. 5. We could measure the spectroscopic redshifts for all galaxies brighter than $B_{450} \simeq 23.0$, apart from object #15, which is located in a region covered by dead fibers. The redshift survey is complete down to $V_{606} \sim 22.5$, where we could determine redshifts for about half of the objects in the f.o.v. In Fig. 6 we plot the color–magnitude diagram for all the objects within the VIMOS-IFU f.o.v. detected on the *HST* data. Redshifts could be measured for almost all the galaxies belonging to the cluster red sequence.

In total, 27 galaxies fall in the redshift range $0.21 < z < 0.25$ (including all measurement flags). We used a classical bi-weight distribution method (Beers et al. 1990) to determine the cluster membership and velocity dispersion. By considering 22 galaxies as belonging to the cluster core, we derived a cluster redshift of $z_{\rm cl} = 0.233 \pm 0.003$ (i.e., the median redshift of the assumed cluster members) and a velocity dispersion of $\sigma_{\rm cl} = 960^{+190}_{-120}$ km s^{-1}. The redshift distribution of galaxies in the range $0.21 < z < 0.25$ is shown in Fig. 7. The cD galaxy redshift is $z = 0.2348 \pm 0.0002$,

Table 2. Properties of the lensed systems and red background galaxies magnified by the galaxy cluster. In the redshift column we list the spectroscopic redshift (if measured) or the photometric one. In the last column, the flag of the spectroscopic redshift or the predictions $z_{\rm mod}$ (or the constraints on the redshift) from the strong lensing model are given. Spectroscopic redshifts are obtained by summing all the images in the given lensed system.

ID	α(J2000)	δ(J2000)	B_{450}	Redshift	Notes
multiple image system					
A1	23:51:39.7	–26:04:48.8	20.26	1.0334 ± 0.0003	flag = 4
A2	23:51:40.0	–26:04:52.0	20.62	1.0334 ± 0.0003	flag = 4
A3	23:51:40.6	–26:05:04.0	21.30	1.0334 ± 0.0003	flag = 4
B1	23:51:40.3	–26:05:12.0	25.13	$z_{\rm ph}$ = 1.20 ± 0.12	$z_{\rm mod}$ = 1.25 ± 0.05
B2	23:51:40.0	–26:05:03.5	23.13	–	$z_{\rm mod}$ = 1.25 ± 0.05
B3	23:51:38.3	–26:04:44.3	25.99	–	$z_{\rm mod}$ = 1.25 ± 0.05
C1	23:51:40.6	–26:04:56.0	24.95	1.578 ± 0.004	flag=1, $z_{\rm mod}$ = 1.6 ± 0.1
C2	23:51:40.7	–26:04:59.1	24.86	1.578 ± 0.004	flag=1, $z_{\rm mod}$ = 1.6 ± 0.1
D1	23:51:38.1	–26:04:49.8	24.29	$z_{\rm ph}$ = 3.12 ± 0.10	$z_{\rm mod}$ = 3.2 ± 0.2
D2	23:51:40.3	–26:05:19.4	25.09	$z_{\rm ph}$ = 2.85 ± 0.10	$z_{\rm mod}$ = 3.2 ± 0.2
single image systems					
Ra	23:51:39.4	–26:05:03.3	23.90	0.620 ± 0.003	flag = 1
Rb	23:51:40.0	–26:05:31.5	27.09	$z_{\rm ph}$ = 0.95 ± 0.05	–
Rc	23:51:37.6	–26:05:14.8	23.74	$z_{\rm ph}$ = 1.15 ± 0.05	$z_{\rm mod} < 1.5$

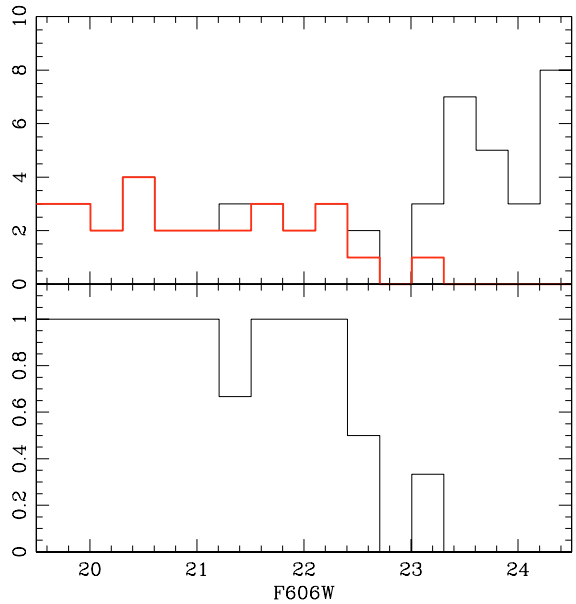

Fig. 5. Completeness of the redshift survey as a function of V-band magnitude (measured in a 2″ aperture). In the *upper panel*, we plot the number of objects detected on the *HST* χ^2-image within the VIMOS-IFU f.o.v. (black line) and the number of those object with measured redshift (red line). In the *lower panel*, the efficiency of the spectroscopic survey is given. The redshift of a bright object at $V \simeq 21.5$ (ID = 15) was not measured since it is located on a set of dead fibers.

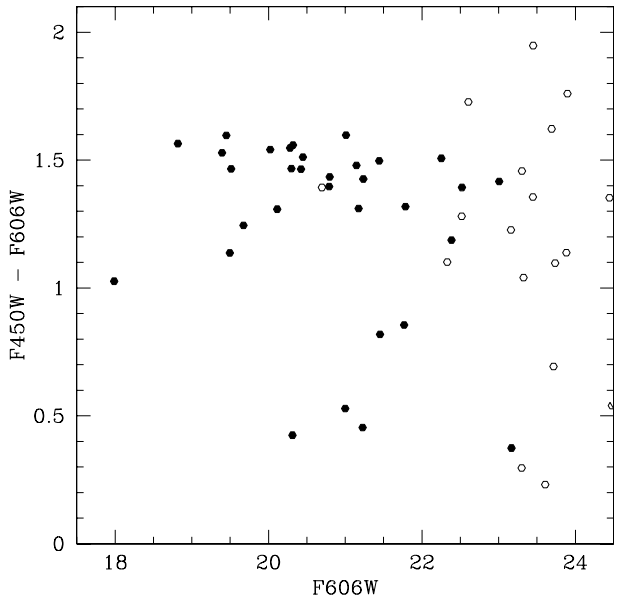

Fig. 6. Color–magnitude relation of the galaxies in VIMOS-IFU f.o.v and detected in the *HST* χ^2-image, using the two WFPC2 pass-bands covering the LR-B spectral range (*F450W* and *F606W*). Filled symbols correspond to objects with measured redshift, empty symbols to objects with no redshift measurement. The cD galaxy (ID = 1) is the brightest object in the diagram. However, becauseof the blue excess associated with the extended emission line region, it lies outside the well-defined cluster red sequence.

which is consistent within the uncertainty with being at rest in the cluster potential well.

All cluster galaxies show the typical features of evolved early-type galaxies (a red continuum with the strong absorption lines characteristic of an evolved stellar population), as expected in the central region of a relaxed cluster. Four representative spectra of cluster members are plotted in Fig. 8. The largest majority of the cluster member shows no strong nebular emission line possibly associated with on-going star formation, except the cD galaxy, which has a rich and spatially extended structure of strong emission lines. In particular, the associated [OII] emission line extends well beyond the galaxy itself (see the blue region visible in Figs. 1 and 4), in regions where the red continuum of the evolved stellar population is barely detected. Further investigation of this spatially extended emission and the cluster galaxies population will be presented in a forthcoming paper.

In Fig. 9 we show the spectra of the three images A1, A2, and A3 forming the giant gravitational arc. The source is a blue star-forming galaxy at redshift 1.0334 ± 0.0003, whose spectrum is characterized by a bright continuum with strong UV absorption lines (FeII and MgII), thus confirming the initial spectroscopic identification of the [OII] emission line by Ebeling et al. (in preparation); see also Sand et al. (2005).

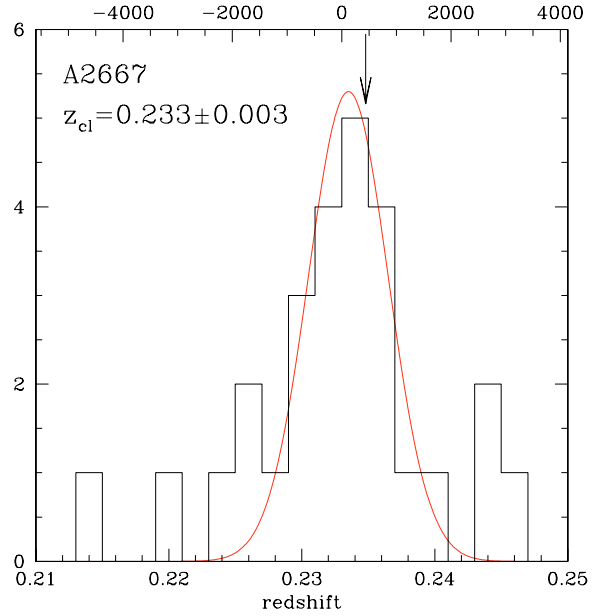

Fig. 7. Redshift distribution of galaxies in the vicinity of the cluster. The bulk of the galaxies are bounded to the cluster centered at $z = 0.233$ with a velocity dispersion of 960 km s^{-1} (overlayed Gaussian profile). The arrow marks the position of the central galaxy. Bin size is $\Delta z = 0.002$, and velocities relative to the cluster rest frame are shown on the top axis (in km s^{-1}).

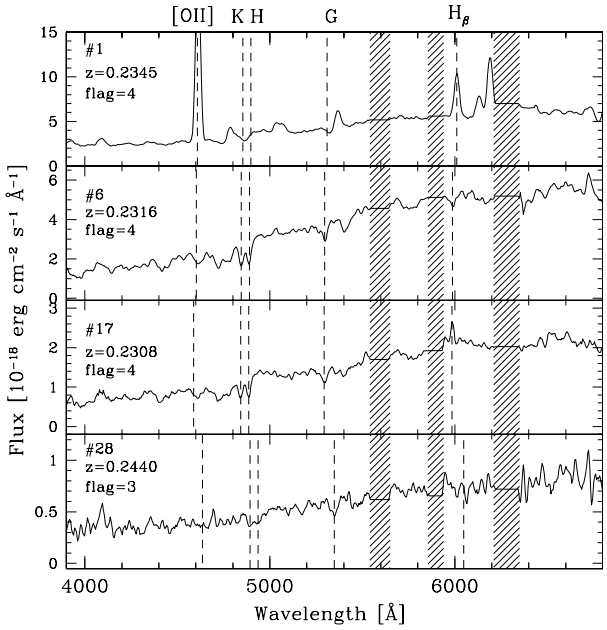

Fig. 8. Four representative spectra of cluster members from the VIMOS-IFU survey of A2667 core, in order of decreasing luminosity. Only a few of the detected lines are indicated. Spectra have been smoothed at the instrumental resolution. Shaded region are strongly affected by sky lines residuals.

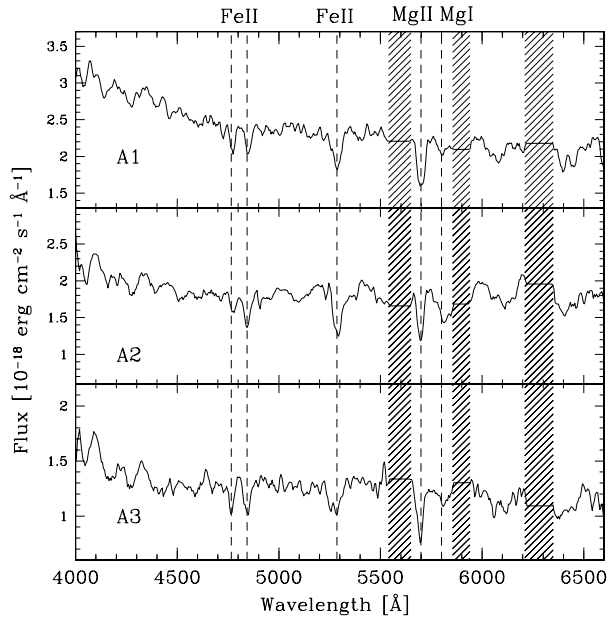

Fig. 9. VIMOS-IFU spectra of the three giant-arc components. Individual spectra are obtained by averaging the flux of the fibers at the image positions. Spectra have been box-car smoothed. Vertical lines show the position of the identified UV absorption features. The redshift of the source is $z_{arc} = 1.0334$. Shaded regions mark the spectral ranges dominated by sky-line residuals.

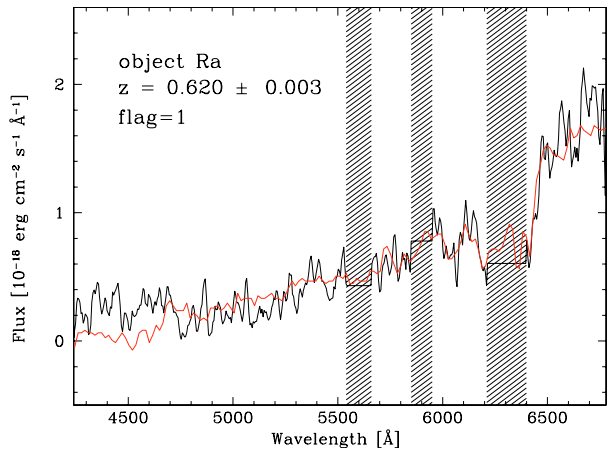

Fig. 10. VIMOS-IFU spectrum of the red object Ra (black line, smoothed at the instrumental resolution), together with a redshifted spectrum of a local early-type galaxy (red line). The spectroscopic redshift is based mainly on the identification of the 4000 Å break.

In Fig. 1 three relatively red, physically unrelated objects are visible: Ra, Rb, Rc. They are not detected in the B_{450} image but are clearly visible in the redder broad-band images. These are background galaxies slightly magnified by the cluster's gravitational field.

The spectrum of the object Ra (see Fig. 10) shows a weak red continuum at wavelengths $\lambda \gtrsim 6000$ Å: the possible identification of the 4000 Å break and the overall shape of the continuum leads to a redshift measurement of $z = 0.62$. Furthermore, the absence of a lensed counterparts allows us to put a firm upper limit of $z \simeq 3.5$.

At the expected position in the VIMOS-IFU data-cube of the other two red objects (Rb and Rc), the continuum at $\lambda \gtrsim 6300$ Å is too noisy to identify any spectral feature unambiguously. The absence of lensed counterparts puts an upper limit on Rc ($z < 1.5$), while Rb is not expected to show multiple images at any redshift location.

Table 3. Parameters of the two fiducial gravitational lensing models[a], assuming individual galaxies with M/L = const. and $M/L \propto L^{0.3}$, respectively. We list the offset between the cluster dark matter halo and the cD galaxy, the axis ratio, the orientation, the core radius, the velocity dispersion, and the truncation radius. See text for details.

Component	ΔRA (arcsec)	ΔDec (arcsec)	a/b	θ (deg)	$r_{\rm core}$ (kpc)	$\sigma_{\rm v}$ (km s^{-1})	$r_{\rm cut}$ (Mpc)
M/L = const.							
cluster halo	–1.6 ± 0.5	–0.5 ± 0.5	0.38	–45	74 ± 8	1004	1.3
L_* galaxy	–	–	–	–	(0.15)	130 ± 7	55 ± 10
$M/L \propto L^{0.3}$							
cluster halo	–0.8 ± 0.5	–1.8 ± 0.5	0.45	–45	76 ± 8	993	1.3
L_* galaxy	–	–	–	–	(0.15)	155 ± 8	70 ± 15

[a] Quantities in parenthesis are not free parameters in the fit.

5. Mass models

5.1. The lensing mass model and redshift prediction of multiple images

To model the mass distribution of this cluster, we used both a cluster mass-scale component (representing the contribution of the dark matter halo and the intra-cluster medium) and cluster-galaxy mass components in a similar way to Kneib et al. (1996); see also Smith et al. (2005). Cluster galaxies were selected according to their redshift (when available, in the inner cluster region covered with VIMOS spectroscopy) or their $J - H$ color, considering galaxies belonging to the cluster red sequence. We also included the lensing contribution from the foreground galaxy #3 ($z = 0.1570 \pm 0.0002$), rescaling its lensing properties at the cluster redshift. In total, the mass distribution model is made of 70 mass components, including the large-scale cluster halo and any cluster galaxies that are brighter than $\simeq 0.05\, L^*_{\rm H}$, a luminosity limit at which their additional contribution is comparable to uncertainties in the overall cluster model.

All model components were parameterized using a smoothly truncated pseudo-isothermal mass distribution model (PIEMD, Kassiola & Kovner 1993), which avoids the unphysical central singularity and infinite spatial extent of the singular isothermal model.

The galaxy mass components were chosen to have the same position, ellipticity and orientation as of their corresponding H-band image. Their mass was scaled to their estimated K-band luminosity, assuming a Faber-Jackson (1976) relation and a global mass-to-light ratio (M/L) that is independent of the galaxy luminosity (see Appendix in Smith et al. 2005). In short, the K-band luminosity was computed by assuming a typical E/S0 spectral energy distribution (redshifted but not corrected for evolution) for the selected cluster galaxies. Moreover, we also used a model in which the mass-to-light ratio has a weak dependence on the luminosity, $M/L \propto L^{0.3}$, as implied by the Fundamental Plane (Jorgensen et al. 1996; see also Natarajan & Kneib 1997).

Using the `lenstool` ray-tracing code (Kneib 1993), we iteratively implemented the constraints from the gravitational lenses. We started by including the triple-imaged giant luminous arc A1, 2, 3. The high-resolution *HST* images show a clear mirror symmetry along this giant arc (fold arc) that gives additional constraints on the location of the critical line at the main arc redshift. Then we used the predictions of the lensing model to find additional lensed systems and include their constraints to improve the model. In particular, we used the position and the morphology of the following fainter multiple images: B1, B2, B3; C1, C2, C3, and D1, D2 (see Fig. 1). The properties of the gravitationally lensed objects and other candidate high-z lensed galaxies in this cluster are summarized in Table 2.

Lensing mass models with $\chi^2 < 1$ are found by fitting the ellipticity, orientation, center, and mass parameters (velocity dispersion, core, and truncation radii) of the cluster-scale component, the truncation radius and the velocity dispersion of the ensemble of cluster galaxies (using the scaling relations for early-type galaxies). The best estimates for these parameters are given in Table 3. In the following we use mass estimates and redshift prediction from the galaxy cluster model that was built after assuming a constant *M/L* for the individual galaxies. However, the predictions of the two models agree within the given errors.

In both mass models we find a small offset between the center of the cD galaxy and the cluster halo component. This agrees with recent findings by Covone et al. (2006b), which analyzed *Chandra* archive data and found an offset between the overall X-ray emission and the central galaxy of less than 1 arcsec.

Finally, the fiducial mass model has been used to derive constraints on the redshift of the other detected multiple images:

1) the very blue low surface brightness B1−B2 arc is predicted at $z = 1.25 \pm 0.05$, which is close to the photometric redshift derived for B1 ($z_{\rm ph} \simeq 1.2$). In the VIMOS-IFU cube, only a noisy spectrum of the second component could be detected, with no useful information to test the model prediction;
2) the blue pair C1−C2 shows a clear mirror symmetry on the *HST* images and is predicted to be located at $z = 1.6 \pm 0.1$. A possible identification of CIV in absorption would lead to $z = 1.578 \pm 0.002$ (flag = 1), very close to the value predicted by the strong lensing model, but a higher S/N spectrum is needed in order to confirm the model's prediction;
3) finally, the objects D1 and D2 are likely to be two images of the same object at $z = 3.2 \pm 0.2$. The model predicts two other counter-images, all of them forming an Einstein cross, but we could not locate these additional 2 images because they are buried under the cD light. Also, unluckily, for this system we could not identify any feature in the noisy VIMOS-IFU spectrum of this object that would have confirmed this redshift prediction, although this time the wavelength coverage was more adequate for searching for the Lyman-α emission line. Therefore, this object has probably no strong Lyman-α emission line.

5.2. Comparison of cluster mass estimates

Our observations and analysis of this cluster allow us to constrain the mass of the cluster core using both dynamical and lensing mass estimates. Assuming a singular isothermal sphere

model, the dynamical mass can be estimated using the relation (see, e.g., Longair 1998)

$$M(<R) = \frac{\pi\sigma^2 R}{G}. \quad (1)$$

Thus for a 30″ radius ($R = 110\,h_{70}^{-1}$ kpc), corresponding to the area covered by our spectroscopic survey, we derive a mass of $M = 7.1^{+3.1}_{-1.7} \times 10^{13}\,h_{70}^{-1}\,M_\odot$.

The mass within the gravitational arc radius is well constrained: $M(<16'') = 2.9 \pm 0.1 \times 10^{13}\,h_{70}^{-1}\,M_\odot$. However, there are some weak degeneracies in the slope of the mass profile in the cluster core. Nevertheless, when extrapolating to $110\,h_{70}^{-1}$ kpc the lensing total mass is $7.2 \pm 0.2 \times 10^{13}\,h_{70}^{-1}\,M_\odot$, a value very close to the dynamical mass estimate.

While the present sample of redshift measurements does not allow a conclusive analysis of the whole cluster dynamical state, the present result supports the hypothesis that the cluster inner region is in hydrostatic equilibrium.

Assuming that the cluster follows the σ–T_X relation (e.g., Girardi et al. 1996), the X-ray temperature of $T_X = 5.95^{+0.42}_{-0.23}$ keV observed by *ASCA* (Ota & Mitsuda 2004) corresponds to a velocity dispersion of 1000^{+190}_{-165} km s^{-1}, which is in good agreement with both our lensing and dynamical estimates. This also agrees with the Allen et al. (1998) findings that galaxy clusters with centrally peaked X-ray emission and a short cooling time generally show good agreement between lensing and X-ray mass estimates.

The agreement between the given dynamical and non-dynamical mass estimates further confirms that the core of A2667 is a relaxed system. Moreover, we note that the dynamical state of A2667 appears to be well predicted by its intra-cluster medium (ICM) temperature. Indeed, Cypriano et al. (2004) suggests that the ICM temperature is a good diagnostic for the dynamical state of an X-ray bright galaxy cluster: galaxy clusters with X-ray temperature below ∼8 keV are likely to be relaxed systems, hence with good agreement between dynamical and non-dynamical mass estimates (see also Cypriano et al. 2005).

However, we note that the Allen et al. (2003) X-ray mass model, based on the more recent *Chandra* observations, underpredicts the size of the Einstein radius. In fact, converting the NFW parameters of their mass model fit into the Einstein radius for a $z = 1.0334$ source plane, we found $\theta_E = 2.7$ arcsec, which is far from the observed 16 arcsec. This discrepancy is not surprising because of the small concentration ($c = 3$) of the NFW model. Keeping the same value of M_{200}, a value of $c = 5$–6 would match the $\theta_E = 16''$ measured. Not enough constraints close to the center lead to an overestimate of r_s and therefore to lower values of the concentration c and the Einstein radius. By combining strong and weak lensing, Kneib et al. (2003) and Broadhurst et al. (2005) show that NFW models with large concentration can match all lensing constraints. It is possible that a combined strong lensing and X-ray analysis would lead to similar results for A2667, although this is beyond the scope of this paper.

Finally, we have determined the rest-frame K-band total light derived from the available ISAAC photometry as described in Sect. 5.1. Within the $110\,h_{70}^{-1}$ kpc aperture, we found a luminosity of $L_K = 1.2 \pm 0.1 \times 10^{12}\,h_{70}^{-2}\,L_\odot$. Hence, we derived an M/L_K ratio of $61 \pm 6\,h_{70}\,M_\odot/L_\odot$. This value is similar to the $z \simeq 0$ measurement obtained by Rines et al. (2004). They have studied the M/L_K radial profile in a sample of nine nearby, X-ray luminous galaxy clusters. On scales of $r \sim 250$ kpc, they measured mass-to-light ratios between 30 and $60\,h_{70}\,M_\odot/L_\odot$.

6. Conclusions

In this paper, we have presented the first integral field spectroscopic survey of a galaxy cluster performed with the VIMOS-IFU. We targeted Abell 2667, a massive, X-ray luminous galaxy cluster at $z = 0.233$, that hosts one of the brightest gravitational arcs in the sky. We obtained a spatially complete spectroscopic survey within the central $\simeq 200\,h_{70}$ kpc that is complete down to $V_{606} \simeq 22.5$. We summarize our main findings here:

1. We have obtained spectroscopic redshift measurements for 34 sources, including 22 cluster members in the cluster core and the three images of the gravitational arc ($z = 1.0334$).
2. We used the position and measured redshift of the giant arc A and the position and morphology of the multiple images B1–B2–B3, the extended triple object C1–C2–C3, and D1–D2 to build a strong gravitational lensing model of the matter distribution in the central $\sim 200 \times 200\,\mathrm{kpc}^2$ around the cluster center. The strong lensing models derived using two different scaling laws for the cluster galaxy population (M/L = const. and $M/L \propto L^{0.3}$,) give results that agree within the errors. The total mass within the Einstein radius ($r_E = 59.6\,h_{70}^{-1}$ kpc) is $M(<16'') = 2.9 \pm 0.1 \times 10^{13}\,h_{70}^{-1}\,M_\odot$, while the extrapolated value at $110\,h_{70}^{-1}$ kpc is $M = 7.2 \pm 0.2 \times 10^{13}\,h_{70}^{-1}\,M_\odot$, where the error bar includes the weak degeneracies in the slope of the mass profile. Moreover, the strong lensing models find a small offset between the dark matter halo and the position of the cD galaxy ($\Delta = 1.7 \pm 0.5$ arcsec).
3. We used the spectroscopic data for the dynamical analysis of the cluster core, and compared our mass estimates with the ones from recently published X-ray analyses. Within the radius $R = 110\,h_{70}^{-1}$ kpc, the mass derived from the dynamical analysis is $M = 7.1^{+3.1}_{-1.7} \times 10^{13}\,h_{70}^{-1}\,M_\odot$, in very good agreement with the value from the strong lensing model. The velocity dispersion is found to be $\sigma = 960^{+190}_{-120}$ km s^{-1}, which is coherent with the value derived from the observed X-ray temperature after assuming that the cluster follows the σ–T_X relation. However, we caution that, although deep, our spectroscopic survey is confined to a limited linear region of the galaxy cluster, and a more extended redshift survey is warranted in order to define the dynamical status of the galaxy population of the cluster as a whole.
4. The published NFW mass model derived from X-ray measurement (Allen et al. 2003) finds a low value for the concentration c and cannot account for the observed large Einstein radius. This is likely because of the lack of strong constraints in the cluster's central region in the X-ray analysis. Indeed, recent studies of the lensing clusters ClG 0024+17 and A1689 (Kneib et al. 2003; Broadhurst et al. 2005), based on joint weak and strong lensing analyses, have demonstrated that large-concentration NFW models are able to match all the observables.
5. Within a $110\,h_{70}^{-1}$ kpc radius, we find a rest-frame K-band M/L ratio of $61 \pm 5\,h_{70}\,M_\odot/L_\odot$, as expected for an evolved stellar population, and one close to the value found for clusters in the local Universe.

The observed agreement between the dynamical and lensing mass estimates supports the idea that the cluster core is in a relaxed dynamical state, as expected from its regular X-ray morphology (Rizza et al. 1998; Allen et al. 2003) and its ICM temperature (Cypriano et al. 2004). Therefore, the core of A2667 appears to be dynamically evolved, in contrast to a large

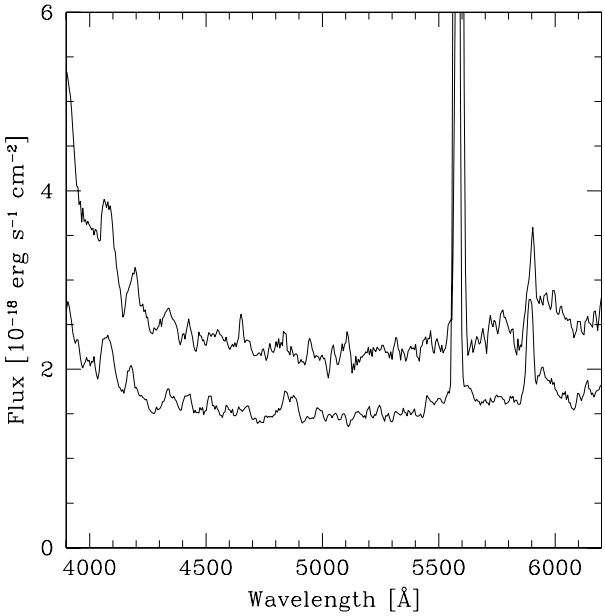

Fig. A.1. The flux limits for the detection of emission lines sources in two different quadrants (Q1, upper curve, and Q2, lower curve) as a function of the wavelength. The curves for the other two quadrants fall between the two plotted here. See text for details.

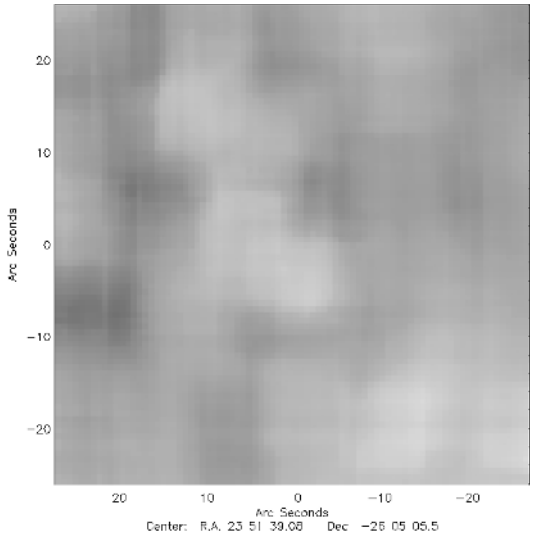

Fig. A.2. 2D map of the sky background rms, considering a window that is $\delta\lambda$ = 40 Å wide at λ = 5000 Å. A logarithmic scale from 10^{-19} to 10^{-18} erg cm^{-2} s^{-1} Å^{-1} is used, with darker grey corresponding to lower sky levels.

fraction (70 ± 20%) of similar X-ray luminous clusters at the same redshift ($z \sim 0.2$, Smith et al. 2005).

This work demonstrates the capabilities of wide f.o.v. integral field spectroscopy in obtaining spatially resolved spectroscopy of extended gravitational arcs and a complete (spatially and in magnitude) survey of the galaxy population in the clusters cores at intermediate redshift. These measurements are useful in understanding the cluster mass distribution properties when using both the strong lensing and dynamical analyses. Wide field IFS is thus a remarkable tool for probing compact sky regions such as the cluster cores targeted here.

Acknowledgements. The authors thank C. Adami, D. Grin, F. La Barbera, S. Brillant, G. P. Smith, and D. Sand for useful comments and discussions, A. Biviano for providing an updated version of the program ROSTAT, and the anonymous referee for comments that helped in improving the presentation of the work. G.C. thanks his wife, Tina, for the enormous patience and invaluable support during all these years. The data published in this paper were reduced using VIPGI, developed by INAF Milano, in the framework of the VIRMOS Consortium activities. G.C. thanks the VIRMOS Consortium team in Milano (B. Garilli, P. Franzetti, M. Scodeggio) for the hospitality during his stays at the IASF and the continuous help on the VIMOS-IFU data reduction. G.C. acknowledges support from the EURO-3D Research Training Network, funded by the European Commission under contract No. HPRN-CT-2002-00305. J.P.K. acknowledges support from the CNRS and Caltech.

Appendix A: Sensitivity and flux limits

While the VIMOS-IFU observations presented here were not meant for a blind search of pure emission-lines objects, it is still interesting to evaluate their sensitivity to faint high-z sources with no detectable continuum, i.e. the limiting flux above which a single emission-line would be detected in our data cube. See also Santos et al. (2004), for a similar discussion of a long-slit search for distant Ly$-\alpha$ sources.

In our datacube, an emission-line could be clearly detected if it covers at least 2 spatial elements and its total flux 3 times the background root-mean-square fluctuations (i.e., the sky background noise). We considered a minimum spectral width of 3 lambda pixels, i.e. about the spectral resolution. We plot the spatially averaged limiting flux of the whole VIMOS-IFU data cube in Fig. A.1 as a function of the wavelength. At the edges of the spectral range, the main contribution comes from the lower sensitivity of the whole instrumental device (telescope, instrument, grism), while in the central regions, where the detection level is more uniform in wavelength, the limiting emission-line flux strongly depends on the atmospheric OH airglow emission. In order to understand the spatial variations of the sensitivity, we show a bi-dimensional map in Fig. A.2 of the defined limiting emission-line flux at $\lambda \simeq 5000$ Å.

The present observations were not conducted with the best strategy: an observational sequence of a larger number of dithered pointings with smaller exposure time would have been more effective in removing spatial non-uniformity, thus improving the final flux limit.

References

Abell, G. O. 1958, ApJS, 3, 211
Allen, S. W. 1998, MNRAS, 296, 392
Allen, S. W., Schmidt, R. W., Fabian, A. C., et al. 2003, MNRAS, 342, 287
Beers, T. C., Flynn, K., & Gebhardt, K. 1990, AJ, 100, 32
Bertin, E., & Arnouts, S. 1996, A&AS, 117, 393
Biviano, A. 2000, in Constructing the Universe with Clusters of Galaxies, IAP 2000 meeting, ed. F. Durret, & D. Gerbal, http://nedwww.ipac.caltech.edu/level5/Biviano2/frames.html
Broadhurst, T., Takada, M., Umetsu, K., et al. 2005, ApJ, 619, L143
Caccianiga, A., Maccacaro, T., Wolter, A., et al. 2000, A&AS, 144, 247
Campusano, L. E., Pelló, R., Kneib, J.-P., et al. 2001, A&A, 378, 394
Condon, J. J., Cotton, W. D., Greisen, E. W., et al. 1998, AJ, 115, 1693
Covone, G., Kneib, J.-P., Soucail, G., et al. 2006a, in Sciences Perspectives for 3D Spectroscopy. ESO Astrophysics Symposia, ed. M. Kissler-Patig, M. M. Roth, & J. R. Walsh [arXiv:astro-ph/0601387]
Covone, G., Adami, C., Durret, F., et al. 2006b, A&A, accepted, preprint [arXiv:astro-ph/0605363]
Cypriano, E. S., Sodré, L., Jr., Kneib, J.-P., & Campusano, L. E. 2004, ApJ, 613, 95
Cypriano, E. S., Lima Neto, G. B., Sodré, L., Jr., et al. 2005, ApJ, 630, 38
D'Odorico, S., Aguayo, A.-M., Brillant, S., et al. 2003, The Messenger, 113, 26
Ebeling, H., Voges, W., Bohringer, H., et al. 1996, MNRAS, 281, 799
Ellis, R. S., Santos, M. R., Kneib, J.-P., & Kuijken, K. 2001, ApJ, 560, L119
Egami, E., Kneib, J.-P., Rieke, G. H., et al. 2005, ApJ, 618, L5

Faber, S. M., & Jackson, R. E. 1976, ApJ, 204, 668
Filippenko, A. V. 1982, PASP, 94, 715
Fruchter, A. S., & Hook, R. N. 2002, PASP, 114, 144
Fukazawa, Y., Makishima, K., & Ohashi, T. 2004, PASJ, 56, 965
Girardi, M., Fadda, D., Giuricin, G., et al. 1996, ApJ, 457, 61
Golse, G., Kneib, J.-P., & Soucail, G. 2002, A&A, 387, 788
Kassiola, A., & Kovner, I. 1993, ApJ, 417, 450
Kissler-Patig, M., et al. 2004, AN, 325, 159
Kneib, J.-P. 1993, Ph.D. Thesis, Université Paul Sabatier, Toulouse
Kneib, J.-P., Ellis, R. S., Smail, I., Couch, W. J., & Sharples, R. M. 1996, ApJ, 471, 643
Kneib, J.-P., Hudelot, P., Ellis, R. S., et al. 2003, ApJ, 598, 804
Kneib, J.-P., van der Werf, P. P., Kraiberg Knudsen, K., et al. 2004a, MNRAS, 349, 1211
Kneib, J.-P., Ellis, R. S., Santos, M. R., & Richard, J. 2004b, ApJ, 607, 697
Kurtz, M. J., Mink, D. J., & Wyatt, W. F. 1992, ADASS, 1, 432
Horne, K. 1986, PASP, 98, 609
Jorgensen, I., Franx, M., & Kjaergaard, P. 1996, MNRAS, 280, 167
Le Fèvre, O., Crampton, D., Lilly, S. J., Hammer, F., & Tresse, L. 1995, ApJ, 455, 60
Le Fèvre, O., Vettolani, G., Maccagni, D., et al. 2003, The Messenger, 111, 18
Longair, M. S. 1998, Galaxy Formation (Springer-Verlag)
Lynds, R., & Petrosian, V. 1986, BAAS, 18, 1014
Natarajan, P., & Kneib, J.-P. 1997, MNRAS, 287, 833
Navarro, J. F., Frenk, C. S., & White, S. D. M. 1996, ApJ, 462, 563
Nolthenius, R., & White, S. D. M. 1987, MNRAS, 225, 505
Ota, N., & Mitsuda, K. 2004, A&A, 428, 757
Rizza, E., Burns, J. O., Ledlow, M. J., et al. 1998, MNRAS, 301, 328
Rines, K., Geller, M. J., Diaferio, A., et al. 2004, AJ, 128, 1078
Sánchez, S. F. 2004, AN, 325, 167
Saslaw, W. C. 1985, ApJ, 297, 49
Sand, D. J., Treu, T., Smith, G. P., & Ellis, R. S. 2004, ApJ, 604, 88
Sand, D. J., Treu, T., Ellis, R. S., & Smith, G. P. 2005, ApJ, 627, 32
Santos, M. R., Ellis, R. S., Kneib, J.-P., et al. 2004, ApJ, 606, 683
Scodeggio, M., Franzetti, P., Garilli, B., et al. 2005, PASP, 117, 1284
Smith, G. P., Kneib, J.-P., Smail, I., et al. 2005, MNRAS, 359, 417
Soucail, G., Fort, B., Mellier, Y., & Picat, J. P. 1987, A&A, 172, L14
Soucail, G., Mellier, Y., Fort, B., et al. 1988, A&A, 191, L19
Soucail, G., Kneib, J.-P., & Golse, G. 2004, A&A, 417, L33
Zanichelli, A., Garilli, B., Scodeggio, M., et al. 2005, PASP, 117, 1271